Measurement of e+e- → Λ Λ ¯ η from 3.5106 to 4.6988 GeV and study of Λ Λ ¯ mass threshold enhancement

BESIII Collaboration; Kalantar-Nayestanaki, N.; Kappert, R.; Kavatsyuk, M.; Messchendorp, J.; Rodin, V.

Published in:
Physical Review D

DOI:
10.1103/PhysRevD.107.112001

Publication date:
2023

Measurement of $e^+e^- \to \Lambda\bar{\Lambda}\eta$ from 3.5106 to 4.6988 GeV and study of $\Lambda\bar{\Lambda}$ mass threshold enhancement

Wei Xu,[1,60] M. Ablikim,[1] M. N. Achasov,[12,b] P. Adlarson,[72] M. Albrecht,[4] R. Aliberti,[33] A. Amoroso,[71a,71c] M. R. An,[37] Q. An,[68,55] Y. Bai,[54] O. Bakina,[34] R. Baldini Ferroli,[27a] I. Balossino,[28a] Y. Ban,[44,g] V. Batozskaya,[1,42] D. Becker,[33] K. Begzsuren,[30] N. Berger,[33] M. Bertani,[27a] D. Bettoni,[28a] F. Bianchi,[71a,71c] E. Bianco,[71a,71c] J. Bloms,[65] A. Bortone,[71a,71c] I. Boyko,[34] R. A. Briere,[5] A. Brueggemann,[65] H. Cai,[73] X. Cai,[1,55] A. Calcaterra,[27a] G. F. Cao,[1,60] N. Cao,[1,60] S. A. Cetin,[59a] J. F. Chang,[1,55] W. L. Chang,[1,60] G. R. Che,[41] G. Chelkov,[34,a] C. Chen,[41] Chao Chen,[52] G. Chen,[1] H. S. Chen,[1,60] M. L. Chen,[1,55,60] S. J. Chen,[40] S. M. Chen,[58] T. Chen,[1,60] X. R. Chen,[29,60] X. T. Chen,[1,60] Y. B. Chen,[1,55] Z. J. Chen,[24,h] W. S. Cheng,[71c] S. K. Choi,[52] X. Chu,[41] G. Cibinetto,[28a] F. Cossio,[71c] J. J. Cui,[47] H. L. Dai,[1,55] J. P. Dai,[76] A. Dbeyssi,[18] R. E. de Boer,[4] D. Dedovich,[34] Z. Y. Deng,[1] A. Denig,[33] I. Denysenko,[34] M. Destefanis,[71a,71c] F. De Mori,[71a,71c] Y. Ding,[32] Y. Ding,[38] J. Dong,[1,55] L. Y. Dong,[1,60] M. Y. Dong,[1,55,60] X. Dong,[73] S. X. Du,[78] Z. H. Duan,[40] P. Egorov,[34,a] Y. L. Fan,[73] J. Fang,[1,55] S. S. Fang,[1,60] W. X. Fang,[1] Y. Fang,[1] R. Farinelli,[28a] L. Fava,[71b,71c] F. Feldbauer,[4] G. Felici,[27a] C. Q. Feng,[68,55] J. H. Feng,[56] K Fischer,[66] M. Fritsch,[4] C. Fritzsch,[65] C. D. Fu,[1] H. Gao,[60] Y. N. Gao,[44,g] Yang Gao,[68,55] S. Garbolino,[71c] I. Garzia,[28a,28b] P. T. Ge,[73] Z. W. Ge,[40] C. Geng,[56] E. M. Gersabeck,[64] A Gilman,[66] K. Goetzen,[13] L. Gong,[38] W. X. Gong,[1,55] W. Gradl,[33] M. Greco,[71a,71c] L. M. Gu,[40] M. H. Gu,[1,55] Y. T. Gu,[15] C. Y Guan,[1,60] A. Q. Guo,[29,60] L. B. Guo,[39] R. P. Guo,[46] Y. P. Guo,[11,f] A. Guskov,[34,a] W. Y. Han,[37] X. Q. Hao,[19] F. A. Harris,[62] K. K. He,[52] K. L. He,[1,60] F. H. Heinsius,[4] C. H. Heinz,[33] Y. K. Heng,[1,55,60] C. Herold,[57] G. Y. Hou,[1,60] Y. R. Hou,[60] Z. L. Hou,[1] H. M. Hu,[1,60] J. F. Hu,[53,i] T. Hu,[1,55,60] Y. Hu,[1] G. S. Huang,[68,55] K. X. Huang,[56] L. Q. Huang,[29,60] X. T. Huang,[47] Y. P. Huang,[1] Z. Huang,[44,g] T. Hussain,[70] N Hüsken,[26,33] W. Imoehl,[26] M. Irshad,[68,55] J. Jackson,[26] S. Jaeger,[4] S. Janchiv,[30] E. Jang,[52] J. H. Jeong,[52] Q. Ji,[1] Q. P. Ji,[19] X. B. Ji,[1,60] X. L. Ji,[1,55] Y. Y. Ji,[47] Z. K. Jia,[68,55] P. C. Jiang,[44,g] S. S. Jiang,[37] X. S. Jiang,[1,55,60] Y. Jiang,[60] J. B. Jiao,[47] Z. Jiao,[22] S. Jin,[40] Y. Jin,[63] M. Q. Jing,[1,60] T. Johansson,[72] S. Kabana,[31] N. Kalantar-Nayestanaki,[61] X. L. Kang,[9] X. S. Kang,[38] R. Kappert,[61] M. Kavatsyuk,[61] B. C. Ke,[78] I. K. Keshk,[4] A. Khoukaz,[65] R. Kiuchi,[1] R. Kliemt,[13] L. Koch,[35] O. B. Kolcu,[59a] B. Kopf,[4] M. Kuemmel,[4] M. Kuessner,[4] A. Kupsc,[42,72] W. Kühn,[35] J. J. Lane,[64] J. S. Lange,[35] P. Larin,[18] A. Lavania,[25] L. Lavezzi,[71a,71c] T. T. Lei,[68,k] Z. H. Lei,[68,55] H. Leithoff,[33] M. Lellmann,[33] T. Lenz,[33] C. Li,[41] C. Li,[45] C. H. Li,[37] Cheng Li,[68,55] D. M. Li,[78] F. Li,[1,55] G. Li,[1] H. Li,[68,55] H. B. Li,[1,60] H. J. Li,[19] H. N. Li,[53,i] Hui Li,[41] J. Q. Li,[4] J. S. Li,[56] J. W. Li,[47] Ke Li,[1] L. J Li,[1,60] L. K. Li,[1] Lei Li,[3] M. H. Li,[41] P. R. Li,[36,j,k] S. X. Li,[11] S. Y. Li,[58] T. Li,[47] W. D. Li,[1,60] W. G. Li,[1] X. H. Li,[68,55] X. L. Li,[47] Xiaoyu Li,[1,60] Y. G. Li,[44,g] Z. X. Li,[15] Z. Y. Li,[56] C. Liang,[40] H. Liang,[32] H. Liang,[1,60] H. Liang,[68,55] Y. F. Liang,[51] Y. T. Liang,[29,60] G. R. Liao,[14] L. Z. Liao,[47] J. Libby,[25] A. Limphirat,[57] D. X. Lin,[29,60] T. Lin,[1] B. J. Liu,[1] C. Liu,[32] C. X. Liu,[1] D. Liu,[18,68] F. H. Liu,[50] Fang Liu,[1] Feng Liu,[6] G. M. Liu,[53,i] H. Liu,[36,j,k] H. B. Liu,[15] H. M. Liu,[1,60] Huanhuan Liu,[1] Huihui Liu,[20] J. B. Liu,[68,55] J. L. Liu,[69] J. Y. Liu,[1,60] K. Liu,[1] K. Y. Liu,[38] Ke Liu,[21] L. Liu,[68,55] L. C. Liu,[21] Lu Liu,[41] M. H. Liu,[11,f] P. L. Liu,[1] Q. Liu,[60] S. B. Liu,[68,55] T. Liu,[11,f] W. K. Liu,[41] W. M. Liu,[68,55] X. Liu,[36,j,k] Y. Liu,[36,j,k] Y. B. Liu,[41] Z. A. Liu,[1,55,60] Z. Q. Liu,[47] X. C. Lou,[1,55,60] F. X. Lu,[56] H. J. Lu,[22] J. G. Lu,[1,55] X. L. Lu,[1] Y. Lu,[7] Y. P. Lu,[1,55] Z. H. Lu,[1,60] C. L. Luo,[39] M. X. Luo,[77] T. Luo,[11,f] X. L. Luo,[1,55] X. R. Lyu,[60] Y. F. Lyu,[41] F. C. Ma,[38] H. L. Ma,[1] L. L. Ma,[47] M. M. Ma,[1,60] Q. M. Ma,[1] R. Q. Ma,[1,60] R. T. Ma,[60] X. Y. Ma,[1,55] Y. Ma,[44,g] F. E. Maas,[18] M. Maggiora,[71a,71c] S. Maldaner,[4] S. Malde,[66] Q. A. Malik,[70] A. Mangoni,[27b] Y. J. Mao,[44,g] Z. P. Mao,[1] S. Marcello,[71a,71c] Z. X. Meng,[63] J. G. Messchendorp,[13,61] G. Mezzadri,[28a] H. Miao,[1,60] T. J. Min,[40] R. E. Mitchell,[26] X. H. Mo,[1,55,60] N. Yu. Muchnoi,[12,b] Y. Nefedov,[34] F. Nerling,[18,d] I. B. Nikolaev,[12,b] Z. Ning,[1,55] S. Nisar,[10,l] Y. Niu,[47] S. L. Olsen,[60] Q. Ouyang,[1,55,60] S. Pacetti,[27b,27c] X. Pan,[52] Y. Pan,[54] A. Pathak,[32] Y. P. Pei,[68,55] M. Pelizaeus,[4] H. P. Peng,[68,55] K. Peters,[13,d] J. L. Ping,[39] R. G. Ping,[1,60] S. Plura,[33] S. Pogodin,[34] V. Prasad,[68,55] F. Z. Qi,[1] H. Qi,[68,55] H. R. Qi,[58] M. Qi,[40] T. Y. Qi,[11,f] S. Qian,[1,55] W. B. Qian,[60] Z. Qian,[56] C. F. Qiao,[60] J. J. Qin,[69] L. Q. Qin,[14] X. P. Qin,[11,f] X. S. Qin,[47] Z. H. Qin,[1,55] J. F. Qiu,[1] S. Q. Qu,[58] K. H. Rashid,[70] C. F. Redmer,[33] K. J. Ren,[37] A. Rivetti,[71c] V. Rodin,[61] M. Rolo,[71c] G. Rong,[1,60] Ch. Rosner,[18] S. N. Ruan,[41] A. Sarantsev,[34,c] Y. Schelhaas,[33] C. Schnier,[4] K. Schoenning,[72] M. Scodeggio,[28a,28b] K. Y. Shan,[11,f] W. Shan,[23] X. Y. Shan,[68,55] J. F. Shangguan,[52] L. G. Shao,[1,60] M. Shao,[68,55] C. P. Shen,[11,f] H. F. Shen,[1,60] W. H. Shen,[60] X. Y. Shen,[1,60] B. A. Shi,[60] H. C. Shi,[68,55] J. Y. Shi,[1] Q. Q. Shi,[52] R. S. Shi,[1,60] X. Shi,[1,55] J. J. Song,[19] W. M. Song,[32,1] Y. X. Song,[44,g] S. Sosio,[71a,71c] S. Spataro,[71a,71c] F. Stieler,[33] P. P. Su,[52] Y. J. Su,[60] G. X. Sun,[1] H. Sun,[60] H. K. Sun,[1] J. F. Sun,[19] L. Sun,[73] S. S. Sun,[1,60] T. Sun,[1,60] W. Y. Sun,[32] Y. J. Sun,[68,55] Y. Z. Sun,[1] Z. T. Sun,[47] Y. X. Tan,[68,55] C. J. Tang,[51] G. Y. Tang,[1] J. Tang,[56] Y. A. Tang,[73] L. Y Tao,[69] Q. T. Tao,[24,h] M. Tat,[66] J. X. Teng,[68,55] V. Thoren,[72] W. H. Tian,[49] Y. Tian,[29,60] I. Uman,[59b] B. Wang,[1] B. Wang,[68,55] B. L. Wang,[60] C. W. Wang,[40] D. Y. Wang,[44,g] F. Wang,[69] H. J. Wang,[36,j,k] H. P. Wang,[1,60] K. Wang,[1,55] L. L. Wang,[1] M. Wang,[47] Meng Wang,[1,60] S. Wang,[14] S. Wang,[11,f] T. Wang,[11,f] T. J. Wang,[41] W. Wang,[56] W. H. Wang,[73] W. P. Wang,[68,55] X. Wang,[44,g] X. F. Wang,[36,j,k] X. L. Wang,[11,f] Y. Wang,[58] Y. D. Wang,[43] Y. F. Wang,[1,55,60] Y. H. Wang,[45] Y. Q. Wang,[1] Yaqian Wang,[17,1] Z. Wang,[1,55] Z. Y. Wang,[1,60] Ziyi Wang,[60] D. H. Wei,[14] F. Weidner,[65] S. P. Wen,[1] D. J. White,[64] U. Wiedner,[4] G. Wilkinson,[66] M. Wolke,[72] L. Wollenberg,[4] J. F. Wu,[1,60] L. H. Wu,[1] L. J. Wu,[1,60]

X. Wu,[11,f] X. H. Wu,[32] Y. Wu,[68] Y. J Wu,[29] Z. Wu,[1,55] L. Xia,[68,55] T. Xiang,[44,g] D. Xiao,[36,j,k] G. Y. Xiao,[40] H. Xiao,[11,f] S. Y. Xiao,[1] Y. L. Xiao,[11,f] Z. J. Xiao,[39] C. Xie,[40] X. H. Xie,[44,g] Y. Xie,[47] Y. G. Xie,[1,55] Y. H. Xie,[6] Z. P. Xie,[68,55] T. Y. Xing,[1,60] C. F. Xu,[1,60] C. J. Xu,[56] G. F. Xu,[1] H. Y. Xu,[63] Q. J. Xu,[16] X. P. Xu,[52] Y. C. Xu,[75] Z. P. Xu,[40] F. Yan,[11,f] L. Yan,[11,f] W. B. Yan,[68,55] W. C. Yan,[78] H. J. Yang,[48,e] H. L. Yang,[32] H. X. Yang,[1] Tao Yang,[1] Y. F. Yang,[41] Y. X. Yang,[1,60] Yifan Yang,[1,60] M. Ye,[1,55] M. H. Ye,[8] J. H. Yin,[1] Z. Y. You,[56] B. X. Yu,[1,55,60] C. X. Yu,[41] G. Yu,[1,60] T. Yu,[69] X. D. Yu,[44,g] C. Z. Yuan,[1,60] L. Yuan,[2] S. C. Yuan,[1] X. Q. Yuan,[1] Y. Yuan,[1,60] Z. Y. Yuan,[56] C. X. Yue,[37] A. A. Zafar,[70] F. R. Zeng,[47] X. Zeng,[6] Y. Zeng,[24,h] X. Y. Zhai,[32] Y. H. Zhan,[56] A. Q. Zhang,[1,60] B. L. Zhang,[1,60] B. X. Zhang,[1] D. H. Zhang,[41] G. Y. Zhang,[19] H. Zhang,[68] H. H. Zhang,[56] H. H. Zhang,[32] H. Q. Zhang,[1,55,60] H. Y. Zhang,[1,55] J. J. Zhang,[49] J. L. Zhang,[74] J. Q. Zhang,[39] J. W. Zhang,[1,55,60] J. X. Zhang,[36,j,k] J. Y. Zhang,[1] J. Z. Zhang,[1,60] Jianyu Zhang,[1,60] Jiawei Zhang,[1,60] L. M. Zhang,[58] L. Q. Zhang,[56] Lei Zhang,[40] P. Zhang,[1] Q. Y. Zhang,[37,78] Shuihan Zhang,[1,60] Shulei Zhang,[24,h] X. D. Zhang,[43] X. M. Zhang,[1] X. Y. Zhang,[47] X. Y. Zhang,[52] Y. Zhang,[66] Y. T. Zhang,[78] Y. H. Zhang,[1,55] Yan Zhang,[68,55] Yao Zhang,[1] Z. H. Zhang,[1] Z. L. Zhang,[32] Z. Y. Zhang,[41] Z. Y. Zhang,[73] G. Zhao,[1] J. Zhao,[37] J. Y. Zhao,[1,60] J. Z. Zhao,[1,55] Lei Zhao,[68,55] Ling Zhao,[1] M. G. Zhao,[41] S. J. Zhao,[78] Y. B. Zhao,[1,55] Y. X. Zhao,[29,60] Z. G. Zhao,[68,55] A. Zhemchugov,[34,a] B. Zheng,[69] J. P. Zheng,[1,55] Y. H. Zheng,[60] B. Zhong,[39] C. Zhong,[69] X. Zhong,[56] H. Zhou,[47] L. P. Zhou,[1,60] X. Zhou,[73] X. K. Zhou,[60] X. R. Zhou,[68,55] X. Y. Zhou,[37] Y. Z. Zhou,[11,f] J. Zhu,[41] K. Zhu,[1] K. J. Zhu,[1,55,60] L. X. Zhu,[60] S. H. Zhu,[67] S. Q. Zhu,[40] W. J. Zhu,[11,f] Y. C. Zhu,[68,55] Z. A. Zhu,[1,60] J. H. Zou,[1] and J. Zu[68,55]

(BESIII Collaboration)

[1]*Institute of High Energy Physics, Beijing 100049, People's Republic of China*
[2]*Beihang University, Beijing 100191, People's Republic of China*
[3]*Beijing Institute of Petrochemical Technology, Beijing 102617, People's Republic of China*
[4]*Bochum Ruhr-University, D-44780 Bochum, Germany*
[5]*Carnegie Mellon University, Pittsburgh, Pennsylvania 15213, USA*
[6]*Central China Normal University, Wuhan 430079, People's Republic of China*
[7]*Central South University, Changsha 410083, People's Republic of China*
[8]*China Center of Advanced Science and Technology, Beijing 100190, People's Republic of China*
[9]*China University of Geosciences, Wuhan 430074, People's Republic of China*
[10]*COMSATS University Islamabad, Lahore Campus, Defence Road, Off Raiwind Road, 54000 Lahore, Pakistan*
[11]*Fudan University, Shanghai 200433, People's Republic of China*
[12]*G. I. Budker Institute of Nuclear Physics SB RAS (BINP), Novosibirsk 630090, Russia*
[13]*GSI Helmholtzcentre for Heavy Ion Research GmbH, D-64291 Darmstadt, Germany*
[14]*Guangxi Normal University, Guilin 541004, People's Republic of China*
[15]*Guangxi University, Nanning 530004, People's Republic of China*
[16]*Hangzhou Normal University, Hangzhou 310036, People's Republic of China*
[17]*Hebei University, Baoding 071002, People's Republic of China*
[18]*Helmholtz Institute Mainz, Staudinger Weg 18, D-55099 Mainz, Germany*
[19]*Henan Normal University, Xinxiang 453007, People's Republic of China*
[20]*Henan University of Science and Technology, Luoyang 471003, People's Republic of China*
[21]*Henan University of Technology, Zhengzhou 450001, People's Republic of China*
[22]*Huangshan College, Huangshan 245000, People's Republic of China*
[23]*Hunan Normal University, Changsha 410081, People's Republic of China*
[24]*Hunan University, Changsha 410082, People's Republic of China*
[25]*Indian Institute of Technology Madras, Chennai 600036, India*
[26]*Indiana University, Bloomington, Indiana 47405, USA*
[27a]*INFN Laboratori Nazionali di Frascati, I-00044, Frascati, Italy*
[27b]*INFN Laboratori Nazionali di Frascati, INFN Sezione di Perugia, I-06100, Perugia, Italy*
[27c]*INFN Laboratori Nazionali di Frascati, University of Perugia, I-06100, Perugia, Italy*
[28a]*INFN Sezione di Ferrara, I-44122, Ferrara, Italy*
[28b]*INFN Sezione di Ferrara, University of Ferrara, I-44122, Ferrara, Italy*
[29]*Institute of Modern Physics, Lanzhou 730000, People's Republic of China*
[30]*Institute of Physics and Technology, Peace Avenue 54B, Ulaanbaatar 13330, Mongolia*
[31]*Instituto de Alta Investigacin, Universidad de Tarapac, Casilla 7D, Arica, Chile*
[32]*Jilin University, Changchun 130012, People's Republic of China*
[33]*Johannes Gutenberg University of Mainz, Johann-Joachim-Becher-Weg 45, D-55099 Mainz, Germany*
[34]*Joint Institute for Nuclear Research, 141980 Dubna, Moscow region, Russia*

[35]*Justus-Liebig-Universitaet Giessen, II. Physikalisches Institut, Heinrich-Buff-Ring 16, D-35392 Giessen, Germany*
[36]*Lanzhou University, Lanzhou 730000, People's Republic of China*
[37]*Liaoning Normal University, Dalian 116029, People's Republic of China*
[38]*Liaoning University, Shenyang 110036, People's Republic of China*
[39]*Nanjing Normal University, Nanjing 210023, People's Republic of China*
[40]*Nanjing University, Nanjing 210093, People's Republic of China*
[41]*Nankai University, Tianjin 300071, People's Republic of China*
[42]*National Centre for Nuclear Research, Warsaw 02-093, Poland*
[43]*North China Electric Power University, Beijing 102206, People's Republic of China*
[44]*Peking University, Beijing 100871, People's Republic of China*
[45]*Qufu Normal University, Qufu 273165, People's Republic of China*
[46]*Shandong Normal University, Jinan 250014, People's Republic of China*
[47]*Shandong University, Jinan 250100, People's Republic of China*
[48]*Shanghai Jiao Tong University, Shanghai 200240, People's Republic of China*
[49]*Shanxi Normal University, Linfen 041004, People's Republic of China*
[50]*Shanxi University, Taiyuan 030006, People's Republic of China*
[51]*Sichuan University, Chengdu 610064, People's Republic of China*
[52]*Soochow University, Suzhou 215006, People's Republic of China*
[53]*South China Normal University, Guangzhou 510006, People's Republic of China*
[54]*Southeast University, Nanjing 211100, People's Republic of China*
[55]*State Key Laboratory of Particle Detection and Electronics, Beijing 100049, Hefei 230026, People's Republic of China*
[56]*Sun Yat-Sen University, Guangzhou 510275, People's Republic of China*
[57]*Suranaree University of Technology, University Avenue 111, Nakhon Ratchasima 30000, Thailand*
[58]*Tsinghua University, Beijing 100084, People's Republic of China*
[59a]*Turkish Accelerator Center Particle Factory Group, Istinye University, 34010, Istanbul, Turkey*
[59b]*Turkish Accelerator Center Particle Factory Group, Near East University, Nicosia, North Cyprus, Mersin 10, Turkey*
[60]*University of Chinese Academy of Sciences, Beijing 100049, People's Republic of China*
[61]*University of Groningen, NL-9747 AA Groningen, Netherlands*
[62]*University of Hawaii, Honolulu, Hawaii 96822, USA*
[63]*University of Jinan, Jinan 250022, People's Republic of China*
[64]*University of Manchester, Oxford Road, Manchester, M13 9PL, United Kingdom*
[65]*University of Muenster, Wilhelm-Klemm-Strasse 9, 48149 Muenster, Germany*
[66]*University of Oxford, Keble Road, Oxford OX13RH, United Kingdom*
[67]*University of Science and Technology Liaoning, Anshan 114051, People's Republic of China*
[68]*University of Science and Technology of China, Hefei 230026, People's Republic of China*
[69]*University of South China, Hengyang 421001, People's Republic of China*
[70]*University of the Punjab, Lahore-54590, Pakistan*
[71a]*University of Turin and INFN, University of Turin, I-10125, Turin, Italy*
[71b]*University of Turin and INFN, University of Eastern Piedmont, I-15121, Alessandria, Italy*
[71c]*University of Turin and INFN, INFN, I-10125, Turin, Italy*
[72]*Uppsala University, Box 516, SE-75120 Uppsala, Sweden*
[73]*Wuhan University, Wuhan 430072, People's Republic of China*
[74]*Xinyang Normal University, Xinyang 464000, People's Republic of China*
[75]*Yantai University, Yantai 264005, People's Republic of China*
[76]*Yunnan University, Kunming 650500, People's Republic of China*
[77]*Zhejiang University, Hangzhou 310027, People's Republic of China*
[78]*Zhengzhou University, Zhengzhou 450001, People's Republic of China*

[a]Also at the Moscow Institute of Physics and Technology, Moscow 141700, Russia.
[b]Also at the Novosibirsk State University, Novosibirsk, 630090, Russia.
[c]Also at the NRC "Kurchatov Institute," PNPI, 188300, Gatchina, Russia.
[d]Also at Goethe University Frankfurt, 60323 Frankfurt am Main, Germany.
[e]Also at Key Laboratory for Particle Physics, Astrophysics and Cosmology, Ministry of Education; Shanghai Key Laboratory for Particle Physics and Cosmology; Institute of Nuclear and Particle Physics, Shanghai 200240, People's Republic of China.
[f]Also at Key Laboratory of Nuclear Physics and Ion-beam Application (MOE) and Institute of Modern Physics, Fudan University, Shanghai 200443, People's Republic of China.
[g]Also at State Key Laboratory of Nuclear Physics and Technology, Peking University, Beijing 100871, People's Republic of China.
[h]Also at School of Physics and Electronics, Hunan University, Changsha 410082, China.

(Received 22 November 2022; accepted 7 April 2023; published 1 June 2023)

Using data samples with a total integrated luminosity of approximately 18 fb^{-1} collected by the BESIII detector operating at the Beijing Electron-Positron Collider II, the process $e^+e^- \to \Lambda\bar{\Lambda}\eta$ is studied at center-of-mass energies between 3.5106 and 4.6988 GeV. The Born cross section for the process $e^+e^- \to \Lambda\bar{\Lambda}\eta$ is measured. No significant structure is observed in the Born cross section line shape. An enhancement near the $\Lambda\bar{\Lambda}$ mass threshold is observed for the first time in the process. The structure can be described by an S-wave Breit-Wigner function. Neglecting contribution of excited Λ states and potential interferences, the mass and width are determined to be $(2356 \pm 7 \pm 15)$ MeV/c^2 and $(304 \pm 28 \pm 54)$ MeV, respectively, where the first uncertainties are statistical and the second are systematic.

DOI: 10.1103/PhysRevD.107.112001

I. INTRODUCTION

In 2005, the *BABAR* Collaboration reported a structure, the $Y(4260)$, with a mass around 4.26 GeV/c^2 in the $\pi^+\pi^- J/\psi$ final state via the initial-state radiation (ISR) process $e^+e^- \to \gamma_{\text{ISR}}\pi^+\pi^- J/\psi$ [1]. The observation was confirmed by the CLEO [2] and Belle [3] Collaborations. Given its strong coupling into the charmonium state, it must contain a charm-anticharm quark pair, because of the strong suppression of the heavy quark-antiquark pair creation within quantum chromodynamics [4]. Because the $Y(4260)$ can be produced by a virtual photon from e^+e^- annihilation, it is a vector state with the spin parity J^{PC} of 1^{--}. Above the $D\bar{D}$ threshold, the four vector charmonium states [$\psi(3770)$, $\psi(4040)$, $\psi(4160)$, and $\psi(4415)$] predicted by the potential model [5] have been established [6]. Moreover, the traditional charmonium states dominantly couple to the ground-state open-charm meson pairs instead of hidden charm states [6]. Therefore, the $Y(4260)$ cannot be explained as a traditional charmonium state. A more precise measurement performed by the BESIII Collaboration shows the $Y(4260)$ contains two structures, $Y(4220)$ and $Y(4330)$ [7]. Later, more states with similar properties were observed [8,9]. These Y states, named ψ states in the Particle Data Group (PDG) [6], are good candidates for exotic states, such as glueballs, compact tetraquarks, hybrids, hadrocharmonia, etc. [4]. Some of these interpretations, however, are disfavored by experiment [10]. Light hadron final states of Y decays, such as $\pi^0 p\bar{p}$ [11], $K^0_S K^\pm\pi^\mp$ [12], $K^0_S K^\pm\pi^\mp\pi^0(\eta)$ [13], $\eta\phi\pi^+\pi^-$ [14], $\Xi^-\bar{\Xi}^+$ [15], $2(p\bar{p})$ [16], $\Lambda\bar{\Lambda}$ [17], and $\omega\pi^0$ [18], have been searched for but not yet discovered. Searching for new decay modes of Y states, for instance, $Y \to \Lambda\bar{\Lambda}\eta$, can add more information to our understanding of their inner structure.

Enhancements near the baryon-antibaryon mass threshold have been observed in low-energy $p\bar{p}$ collisions, charmonium decays, and B meson decays. Using PS185 low-energy $p\bar{p}$ collision data, a structure near the $\Lambda\bar{\Lambda}$ threshold was observed with a partial wave analysis of $p\bar{p} \to \Lambda\bar{\Lambda}$ [19]. In charmonium decays, enhancements are observed in $p\bar{p}$ final states of the processes $J/\psi \to \gamma p\bar{p}$ [20]. In B meson decays, enhancements were found in the processes $B^0 \to \Lambda\bar{\Lambda}K^0(K^{*0})$ [21], $B^0 \to p\bar{\Lambda}\pi^-$ [22], $B^+ \to p\bar{p}\pi^+$, $B^0 \to p\bar{p}K^0$ [23], $B^+ \to \Lambda\bar{\Lambda}K^+$ [24], $B^{+(0)} \to p\bar{p}K^{*+(0)}$ [25], $B^0 \to \bar{D}^{*0}p\bar{p}, \bar{D}^0 p\bar{p}$ [26], $B^0 \to p\bar{\Lambda}D^{(*)-}$ [27], $B^0_{(s)} \to p\bar{p}h^+h'^-$ [28], $B^+ \to p\bar{\Lambda}K^+K^-$ [29], $B^0 \to p\bar{p}\pi^0$ [30], $B^+ \to p\bar{p}\mu^+\nu_\mu$ [31], etc. Strikingly, there is no corresponding enhancement observed in $\psi(2S) \to \gamma p\bar{p}$ [32], $\psi(2S) \to p\bar{p}\pi^0$ [33], $\Upsilon(1S) \to \gamma p\bar{p}$ [34], $J/\psi \to \omega p\bar{p}$ [35], $\psi(2S) \to p\bar{p}\eta$ [36], $J/\psi, \psi(2S) \to p\bar{p}\phi$ [37,38], $J/\psi, \psi(2S) \to \eta\Sigma^+\bar{\Sigma}^-$ [39], $\psi(2S) \to \Lambda\bar{\Lambda}\eta(\pi^0)$ [40], $\psi(2S) \to \Lambda\bar{\Lambda}\omega$ [41], $B^+ \to p\bar{p}K^+$ [42], $\bar{B}^0 \to D^0\Lambda\bar{\Lambda}$ [43], $B \to p\bar{p}\pi\pi$ [44] $B^0_s \to J/\psi p\bar{p}$ [45], and $B^- \to J/\psi\Lambda\bar{p}$ [46] decays. Many theory models have been proposed for the interpretation of these enhancements, including a gluonic mechanism [47], a fragmentation mechanism [47], baryonia [48], multiquark states [49], and final-state interactions [50]. Searching for enhancements with different quantum numbers in different reactions can provide more constraints on these models.

In this article, we report a study of the reaction $e^+e^- \to \Lambda\bar{\Lambda}\eta$ with a partial reconstruction technique, based on the data recorded at center-of-mass energies from 3.5106 to

[i]Also at Guangdong Provincial Key Laboratory of Nuclear Science, Institute of Quantum Matter, South China Normal University, Guangzhou 510006, China.
[j]Also at Frontiers Science Center for Rare Isotopes, Lanzhou University, Lanzhou 730000, People's Republic of China.
[k]Also at Lanzhou Center for Theoretical Physics, Lanzhou University, Lanzhou 730000, People's Republic of China.
[l]Also at the Department of Mathematical Sciences, IBA, Karachi, Pakistan.

4.6988 GeV. The Born cross sections are measured, and possible resonances are searched for by fitting the energy-dependent distribution of the Born cross sections. In addition, a threshold enhancement is observed in the $\Lambda\bar{\Lambda}$ mass spectrum. The mass and width of the structure are determined by a fit with an S-wave Breit-Wigner function, and the angular distribution of the structure is studied.

II. DETECTOR AND DATA SAMPLES

The BESIII detector [51] records symmetric e^+e^- collisions provided by the Beijing Electron-Positron Collider II (BEPCII) storage ring [52], which operates in the center-of-mass energy range from 2.00 to 4.95 GeV. The cylindrical core of the BESIII detector covers 93% of the full solid angle and consists of a helium-based multilayer drift chamber (MDC), a plastic scintillator time-of-flight system (TOF), and a CsI(Tl) electromagnetic calorimeter (EMC), which are all enclosed in a superconducting solenoidal magnet providing a 1.0 T magnetic field. The solenoid is supported by an octagonal flux-return yoke with resistive plate counter muon identification modules interleaved with steel. The charged-particle momentum resolution at 1 GeV/c is 0.5%, and the dE/dx resolution is 6% for electrons from Bhabha scattering. The EMC measures photon energies with a resolution of 2.5% (5%) at 1 GeV in the barrel (end cap) region. The time resolution in the TOF barrel region is 68 ps, while that in the end cap region is 110 ps. The end cap TOF system was upgraded in 2015 using multigap resistive plate chamber technology, providing a time resolution of 60 ps [53].

Simulated data samples produced with GEANT4-based [54] Monte Carlo (MC) software, which includes the geometric description of the BESIII detector and the detector response, are used to determine detection efficiencies and to estimate background contributions. The simulation includes the beam energy spread and ISR in the e^+e^- annihilations modeled with the generator KKMC [55]. The inclusive MC sample includes the production of open-charm processes, the ISR production of vector charmonium(like) states, and the continuum processes incorporated in KKMC [55]. All particle decays are modeled with EVTGEN [56] using branching fractions either taken from the PDG [6], when available, or otherwise estimated with LUNDCHARM [57]. Final-state radiation from charged final-state particles is incorporated using PHOTOS [58]. At each energy point, we generate a signal MC sample of three-body process $e^+e^- \to \Lambda\bar{\Lambda}\eta$ with $\eta \to \gamma\gamma$ using a uniformly distributed phase space (PHSP) model. The MC sample for the study of threshold enhancement is discussed in Sec. V.

III. EVENT SELECTION

The signal candidates of the process $e^+e^- \to \Lambda\bar{\Lambda}\eta$ are selected with a partial reconstruction technique, to achieve higher efficiency. This technique requires that only the Λ ($\bar{\Lambda}$) baryon and η meson are reconstructed, inferring the $\bar{\Lambda}$ (Λ) from energy-momentum conservation. Thanks to the partial reconstruction technique, the efficiency is improved by about a factor of 2 compared to the full reconstruction. The Λ ($\bar{\Lambda}$) candidates and the η candidates are reconstructed with $p\pi^-$ ($\bar{p}\pi^+$) and $\gamma\gamma$ decay modes, respectively.

Charged tracks detected in the MDC are required to be within a polar angle (θ) range of $|\cos\theta| < 0.93$, where θ is defined with respect to the z axis, the symmetry axis of the MDC. The distance of the closest approach to the interaction point (IP) along the z axis must be less than 20 cm. Particle identification (PID) for charged tracks combines measurements of dE/dx in the MDC and the flight time in the TOF to form likelihoods for each hadron (pion, kaon, and proton) hypothesis. Tracks are identified as protons (pions) when the proton (pion) hypothesis has the largest likelihood. Proton and pion track pairs with opposite charges are constrained to originate from a common vertex to form the Λ ($\bar{\Lambda}$) candidates by a vertex fit [59]. The obtained χ^2 in the fit, denoted as $\chi^2_{\rm vtx}$, are kept for further analysis. The decay length of the Λ ($\bar{\Lambda}$) candidate is required to be greater than twice the vertex resolution away from the IP.

Photon candidates are identified using showers in the EMC. The deposited energy of each shower must be more than 25 MeV in the barrel region ($|\cos\theta| < 0.80$) and more than 50 MeV in the end cap region ($0.86 < |\cos\theta| < 0.92$). To exclude showers that originate from charged tracks identified as antiprotons, the angle subtended by the EMC shower and the position of the closest charged track at the EMC must be greater than 20° as measured from the IP. The angle is required to be greater than 10° for other types of charged tracks. To suppress electronic noise and showers unrelated to the event, the difference between the EMC time and the event start time is required to be within [0, 700] ns. To remove fake photons from neutron-antineutron annihilations, $E_{3\times3}/E_{5\times5}$ and the lateral moment [60] describing the shape of electromagnetic showers are required to be greater than 0.85 and less than 0.4, respectively, where $E_{3\times3}$ ($E_{5\times5}$) is the total energy deposited in the 3×3 (5×5) crystals around the seed of the shower [61]. Photon pairs are used to reconstruct $\eta \to \gamma\gamma$ decays.

To suppress the background and improve the momentum resolution, a one-constraint (1C) kinematic fit [62] under the hypothesis $e^+e^- \to \gamma\gamma p\pi^-\bar{p}\pi^+$ is performed with the recoil mass against $\gamma\gamma p\pi^-$ ($\gamma\gamma\bar{p}\pi^+$) constrained to the known mass of Λ, M_Λ [6]. There is more than half of events with multiple reconstructed $\gamma\gamma p\pi^-$ ($\gamma\gamma\bar{p}\pi^+$) candidates in the data. The candidate with the smallest $\chi^2_{\rm vtx} + \chi^2_{\rm 1C}$ is kept, where $\chi^2_{\rm vtx}$ and $\chi^2_{\rm 1C}$ are the χ^2 of the vertex fit and 1C kinematic fit, respectively. We require $\chi^2_{\rm vtx} < 20$ and the $\chi^2_{\rm 1C} < 10$. After the above selection criteria are applied, the invariant mass of the $p\pi^-$ ($\bar{p}\pi^+$) combination is required to satisfy

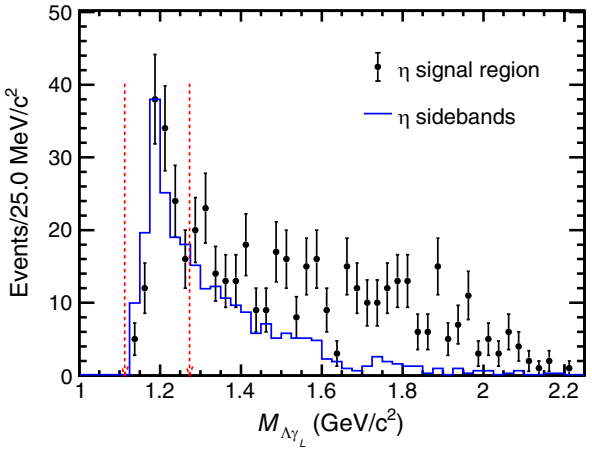

FIG. 1. Distributions of $M_{\Lambda\gamma_L}$ from data in the η signal region (black points with error bars) and the sidebands (blue histogram) at 4.178 GeV, where the η signal region and sidebands are defined in Sec. IV. The dashed red arrows denote the Σ^0 mass region.

$1.112\ \mathrm{GeV}/c^2 < M_{p\pi^-(\bar{p}\pi^+)} < 1.120\ \mathrm{GeV}/c^2$. A study with the inclusive MC sample using TopoAna [63] shows that the main background contributions are from processes with Σ^0 ($\bar{\Sigma}^0$) baryons in the final states. Figure 1 shows the distribution for invariant mass of the Λ and photon with lower energy γ_L from the data. An obvious Σ^0 peak is observed. In order to suppress background from $\Sigma^0 \to \Lambda\gamma_L$ ($\bar{\Sigma}^0 \to \bar{\Lambda}\gamma_L$) decays, the invariant mass of the reconstructed Λ ($\bar{\Lambda}$) and the selected photon with lower energy $M_{\Lambda\gamma_L}$ ($M_{\bar{\Lambda}\gamma_L}$) is required to be outside the Σ^0 ($\bar{\Sigma}^0$) mass region of $[1.113, 1.273]\ \mathrm{GeV}/c^2$. A study of the $M_{\gamma\gamma}$ distribution with the inclusive MC indicates small peaking background contributions from the processes $e^+e^- \to \eta\Sigma^0\bar{\Lambda} + \mathrm{c.c.}$ and $e^+e^- \to \Sigma^0\bar{\Sigma}^0\eta$ near the η peak in the $M_{\gamma\gamma}$ distribution. However, the process $e^+e^- \to \eta\Sigma^0\bar{\Lambda} + \mathrm{c.c.}$ is suppressed because of isospin violation. Due to the two extra photons in the final state, the $e^+e^- \to \Sigma^0\bar{\Sigma}^0\eta$ process is also suppressed by the 1C kinematic fit.

IV. CROSS SECTION MEASUREMENT

The Born cross section of the process $e^+e^- \to \Lambda\bar{\Lambda}\eta$ with contributions from intermediate states at each center-of-mass energy is calculated as

$$\sigma^{\mathrm{Born}} = \frac{N_{\mathrm{sig}}}{\mathcal{L}_{\mathrm{int}}\mathcal{B}\varepsilon(1+\delta)(1+\delta^v)}, \quad (1)$$

where N_{sig} is the signal yield, $\mathcal{L}_{\mathrm{int}}$ is the integrated luminosity measured using large-angle Bhabha events [64–66], $\mathcal{B}$ is the product of the branching fractions of $\eta \to \gamma\gamma$ and $\Lambda \to p\pi^-$ ($\bar{\Lambda} \to \bar{p}\pi^+$) decays from the PDG [6], ε is the reconstruction efficiency determined by MC simulation, $(1+\delta)$ is the ISR correction factor, and $(1+\delta^v)$ is the vacuum polarization factor [67].

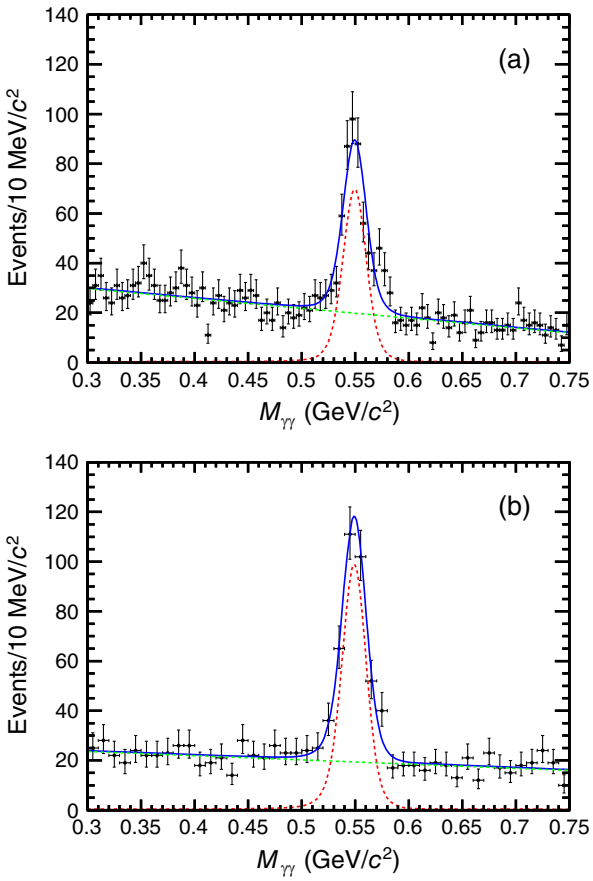

FIG. 2. Fits to the invariant mass spectra of $\gamma\gamma$ for the events surviving the selection criteria at (a) $\sqrt{s} = 3.7730$ and (b) $\sqrt{s} = 4.1784$ GeV. The black points with error bars are data. The solid blue, dashed red, and dashed green lines correspond to the fit result, signal, and background, respectively.

The signal yield is determined by an unbinned maximum-likelihood fit to the $M_{\gamma\gamma}$ spectrum at each energy point. The background is modeled by a linear function. The signal is described by an MC-simulated shape convolved with a Gaussian function which is used to compensate for the differences in resolution between the MC simulation and the data. The means of the Gaussian functions at different energy points are free. The widths of the Gaussian functions cannot be constrained by data samples with low luminosities. Therefore, they are fixed to a common value obtained from the fit of the largest data sample taken at $\sqrt{s} = 3.7730$ GeV. Figure 2 shows the fit results for the data at $\sqrt{s} = 4.1784$ GeV. The number of signal events in the η signal region ($0.521 < M_{\gamma\gamma} < 0.572\ \mathrm{GeV}/c^2$) for each energy point is determined by integrating the fitted signal shape in the signal region and is summarized in Table I. The contribution of peaking background mentioned in Sec. III is estimated to be 1.34% at $\sqrt{s} = 4.1784$ GeV by adding the shape derived from the MC simulation of the

TABLE I. Born cross sections at the 31 energy points for the process $e^+e^- \to \Lambda\bar{\Lambda}\eta$, where $\sqrt{s}$ [65,66,68] is the center-of-mass energy, $\mathcal{L}_{\rm int}$ is the integrated luminosity [64–66], signal yield is the number of signal events in the signal region where the uncertainty is statistical only, ε is the reconstruction efficiency after the ISR correction where the uncertainty is from the limited data sample sizes, $(1+\delta)$ and $(1+\delta^v)$ are the ISR correction factor and vacuum polarization factor, respectively, and σ is the Born cross section where the first uncertainty is statistical and the second is systematic.

$\sqrt{s}$ (GeV)	$\mathcal{L}_{\rm int}$ (pb^{-1})	Signal yield	ε (%)	$(1+\delta)$	$(1+\delta^v)$	σ (pb)
3.5106	458.7	80.3 ± 11.0	15.6 ± 0.2	0.864	1.045	$3.13 \pm 0.43 \pm 0.18$
3.7730	2916.9	378.9 ± 24.1	18.4 ± 0.1	0.948	1.059	$1.77 \pm 0.11 \pm 0.10$
3.8720	219.2	15.8 ± 5.1	17.4 ± 0.8	0.991	1.050	$1.00 \pm 0.32 \pm 0.07$
4.0076	482.0	64.1 ± 9.0	18.8 ± 0.5	0.979	1.046	$1.77 \pm 0.25 \pm 0.11$
4.1285	401.5	36.4 ± 7.0	18.0 ± 0.5	1.054	1.053	$1.17 \pm 0.23 \pm 0.08$
4.1574	408.7	37.1 ± 7.0	19.6 ± 0.6	1.057	1.054	$1.09 \pm 0.21 \pm 0.07$
4.1784	3189.0	277.4 ± 19.5	20.2 ± 0.3	1.054	1.055	$1.00 \pm 0.07 \pm 0.06$
4.1888	570.0	39.8 ± 7.5	19.0 ± 0.6	1.083	1.057	$0.82 \pm 0.15 \pm 0.06$
4.1989	526.0	63.2 ± 8.8	20.0 ± 0.5	1.055	1.057	$1.38 \pm 0.19 \pm 0.09$
4.2092	517.1	42.9 ± 7.7	19.1 ± 0.6	1.039	1.057	$1.00 \pm 0.18 \pm 0.06$
4.2187	569.2	47.0 ± 7.8	17.7 ± 0.6	1.097	1.057	$1.06 \pm 0.17 \pm 0.07$
4.2263	1100.9	80.6 ± 10.3	20.7 ± 0.5	1.048	1.057	$0.81 \pm 0.10 \pm 0.05$
4.2357	530.3	41.5 ± 7.5	20.3 ± 0.7	1.060	1.055	$0.89 \pm 0.16 \pm 0.06$
4.2438	538.1	48.6 ± 8.0	20.0 ± 0.7	1.085	1.056	$1.01 \pm 0.17 \pm 0.07$
4.2580	828.4	58.7 ± 8.9	19.9 ± 0.6	1.060	1.054	$0.79 \pm 0.12 \pm 0.05$
4.2668	531.1	39.1 ± 7.4	19.1 ± 0.9	1.029	1.053	$0.91 \pm 0.17 \pm 0.07$
4.2879	502.4	46.9 ± 7.5	20.9 ± 0.6	1.000	1.053	$1.05 \pm 0.17 \pm 0.07$
4.3121	501.2	40.0 ± 7.3	18.6 ± 0.7	1.026	1.052	$1.04 \pm 0.19 \pm 0.07$
4.3374	505.0	44.6 ± 7.4	20.0 ± 0.6	1.020	1.051	$1.06 \pm 0.17 \pm 0.07$
4.3583	543.9	53.6 ± 7.8	20.3 ± 0.6	1.058	1.051	$1.11 \pm 0.16 \pm 0.07$
4.3774	522.7	27.1 ± 6.0	20.4 ± 0.8	1.114	1.051	$0.58 \pm 0.13 \pm 0.04$
4.3964	507.8	25.2 ± 5.9	17.7 ± 0.9	1.141	1.052	$0.58 \pm 0.13 \pm 0.05$
4.4156	1090.7	72.1 ± 9.8	20.5 ± 0.6	1.092	1.053	$0.72 \pm 0.10 \pm 0.05$
4.4400	569.9	36.5 ± 7.0	19.7 ± 0.7	0.943	1.055	$0.81 \pm 0.15 \pm 0.08$
4.4671	111.1	13.4 ± 3.9	23.0 ± 1.3	0.913	1.055	$1.36 \pm 0.39 \pm 0.14$
4.5995	586.9	36.4 ± 6.7	21.3 ± 0.9	1.122	1.055	$0.61 \pm 0.11 \pm 0.05$
4.6280	521.5	31.5 ± 6.3	18.5 ± 0.8	1.133	1.055	$0.69 \pm 0.14 \pm 0.05$
4.6612	529.6	31.6 ± 6.1	20.3 ± 1.0	1.119	1.056	$0.48 \pm 0.12 \pm 0.04$
4.6409	552.4	22.9 ± 5.5	17.1 ± 0.8	1.205	1.056	$0.63 \pm 0.12 \pm 0.05$
4.6819	1669.3	74.0 ± 9.6	17.2 ± 0.7	1.258	1.056	$0.49 \pm 0.06 \pm 0.04$
4.6988	536.5	23.1 ± 5.5	19.2 ± 1.0	1.188	1.056	$0.45 \pm 0.11 \pm 0.04$

two processes to the nominal fit model. The effect of the peaking background events on the determination of signal yields will be discussed in Sec. VI.

As shown in Fig. 3, evident discrepancies between the background-subtracted data and PHSP MC simulation are seen, where the background contributions are subtracted using the events from the η sidebands, defined as $0.368 < M_{\gamma\gamma} < 0.470$ and $0.622 < M_{\gamma\gamma} < 0.724$ GeV/c^2. To estimate the reconstruction efficiencies, the PHSP MC samples are weighted according to the background-subtracted data distributions of $M_{\Lambda\bar{\Lambda}}$, $M_{\Lambda\eta}$, and $M_{\bar{\Lambda}\eta}$ shown in Fig. 3. Because of limited sample sizes, we cannot determine the exact two-dimensional weighting factors from the $e^+e^- \to \Lambda\bar{\Lambda}\eta$ Dalitz distributions of data. We take the weight for each two-dimensional distribution as the product of the one-dimensional distributions. The distributions of $M_{\Lambda\bar{\Lambda}}$, $M_{\Lambda\eta}$, and $M_{\bar{\Lambda}\eta}$ are treated as independent. Because of this approximation, all combinations of invariant masses among Λ, $\bar{\Lambda}$, and η are taken into account to make the MC simulation consistent with data. Therefore, the weighting factor is calculated as the average of the three two-dimensional distributions

$$\begin{aligned} w^{i=\{m,n,o\}}&(M_{\Lambda\bar{\Lambda}}, M_{\Lambda\eta}, M_{\bar{\Lambda}\eta}) \\ &= \frac{1}{3}\frac{N^{\rm data}_{M_{\Lambda\bar{\Lambda}}}(m)}{N^{\rm MC}_{M_{\Lambda\bar{\Lambda}}}(m)}\frac{N^{\rm data}_{M_{\Lambda\eta}}(n)}{N^{\rm MC}_{M_{\Lambda\eta}}(n)} + \frac{1}{3}\frac{N^{\rm data}_{M_{\Lambda\bar{\Lambda}}}(m)}{N^{\rm MC}_{M_{\Lambda\bar{\Lambda}}}(m)}\frac{N^{\rm data}_{M_{\bar{\Lambda}\eta}}(o)}{N^{\rm MC}_{M_{\bar{\Lambda}\eta}}(o)} \\ &\quad + \frac{1}{3}\frac{N^{\rm data}_{M_{\Lambda\eta}}(n)}{N^{\rm MC}_{M_{\Lambda\eta}}(n)}\frac{N^{\rm data}_{M_{\bar{\Lambda}\eta}}(o)}{N^{\rm MC}_{M_{\bar{\Lambda}\eta}}(o)}, \end{aligned} \tag{2}$$

where w^i is the weight for event i corresponding to bins m, n, and o of the $M_{\Lambda\bar{\Lambda}}$, $M_{\bar{\Lambda}\eta}$ and $M_{\bar{\Lambda}\eta}$ distributions and $N^{\rm data/MC}_{M_{\Lambda\bar{\Lambda}}}(m)$, $N^{\rm data/MC}_{M_{\Lambda\eta}}(n)$, and $N^{\rm data/MC}_{M_{\bar{\Lambda}\eta}}(o)$ are numbers of events in bins m, n, and o of the $M_{\Lambda\bar{\Lambda}}$, $M_{\bar{\Lambda}\eta}$ and $M_{\bar{\Lambda}\eta}$

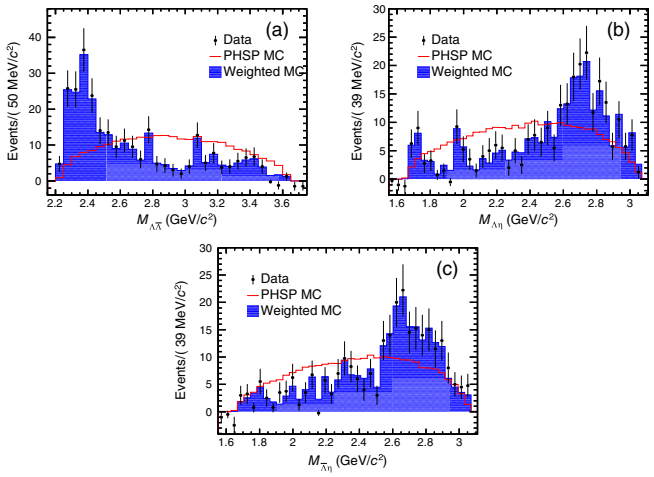

FIG. 3. Distributions of (a) $M_{\Lambda\bar{\Lambda}}$, (b) $M_{\Lambda\eta}$, and (c) $M_{\bar{\Lambda}\eta}$ obtained from events within the η signal region at $\sqrt{s} = 4.1784$ GeV. The black points with error bars are background-subtracted data. The solid (red) histograms and filled (blue) histograms denote the PHSP MC and weighted PHSP MC sample, respectively.

distributions in data and PHSP MC sample. The weighted MC sample is iteratively weighted twice in the same way to achieve better agreement between data and MC simulation. As shown in Fig. 3, the distributions of the weighted PHSP MC sample (filled histograms) are consistent with the background-subtracted data (black points). The efficiencies from the weighted PHSP MC samples are calculated as

$$\varepsilon^{\rm wtd} = \frac{\sum_{i=1}^{N_{\rm rec}} w^i(M_{\Lambda\bar{\Lambda}}, M_{\Lambda\eta}, M_{\bar{\Lambda}\eta})}{\sum_{j=1}^{N_{\rm gen}} w^j(M_{\Lambda\bar{\Lambda}}, M_{\Lambda\eta}, M_{\bar{\Lambda}\eta})}, \tag{3}$$

where $N_{\rm rec}$ and $N_{\rm gen}$ are the numbers of reconstructed events and generated events, respectively, and $w^{i(j)}(M_{\Lambda\bar{\Lambda}}, M_{\Lambda\eta}, M_{\bar{\Lambda}\eta})$ is the weighting factor for event i (j).

In Eq. (2), data are used in the calculation of the weighting factor. The statistical uncertainties of the numbers of data events in the intervals of the background-subtracted data distributions propagate to the weighting factor and contribute to the uncertainty of the efficiency [see Eq. (3)] which will be considered in Sec. VI.

To evaluate ε after the ISR correction and $(1+\delta)$, an iterative procedure is performed [69]. The initial value of ε for the initial line shape is obtained by the weighted PHSP MC sample. The initial value of $(1+\delta)$ is determined by KKMC with the line shape assumed to be flat. The locally weighted scatterplot smoothing (LOWESS) method [70] is used to smooth the line shape. The iterative procedure is repeated until the ratio of the measured cross section to the corresponding value from previous iteration is consistent with one within the statistical uncertainty. Table I summarizes the ε values after ISR correction and $(1+\delta)$ for each energy point.

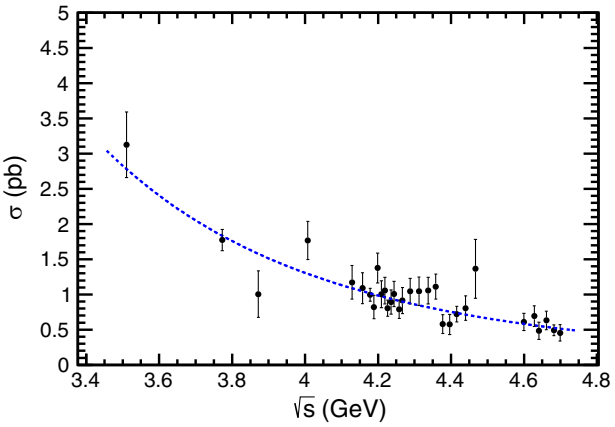

FIG. 4. Measured Born cross sections of the process $e^+e^- \to \Lambda\bar{\Lambda}\eta$ at $\sqrt{s}$ from 3.5106 to 4.6988 GeV indicated by the black points with error bars (combined statistical and systematic uncertainties). The dashed blue line is the fit result.

Table I also summarizes the measured Born cross sections at the 31 energy points. To search for possible resonances decaying into $\Lambda\bar{\Lambda}\eta$, the least-squares method is used to perform the fit of the Born cross sections with both statistical and systematic uncertainties taken into account, ignoring the correlation between the different energy points. The continuum production of $e^+e^- \to \Lambda\bar{\Lambda}\eta$ can be well described by a power-law function $\sigma_{\rm con} = C/s^{\lambda}$ [71]. Figure 4 shows the fit to the Born cross section. The fit with the power-law function yields the goodness of fit $\chi^2/{\rm ndf} = 29.9/29$, where ndf denotes the number of degrees of freedom. The corresponding p value is 0.418. The fitted parameters C and λ are $(4.0 \pm 2.5) \times 10^3$ GeV$^{2\lambda}$ pb and 2.9 ± 0.2, respectively.

V. STUDY OF $\Lambda\bar{\Lambda}$ MASS THRESHOLD ENHANCEMENT

As shown in Fig. 5, examinations of the Dalitz plots of the process $e^+e^- \to \Lambda\bar{\Lambda}\eta$ indicate that the threshold enhancement in $\Lambda\bar{\Lambda}$ mass spectra is the dominant component. The enhancement can also be observed near the $\Lambda\bar{\Lambda}$ mass threshold as shown in Fig. 6. This structure cannot be described by the PHSP MC simulation. To confirm the existence of the structure, we study the $\Lambda\bar{\Lambda}$ invariant mass spectra of the events in which the Λ, $\bar{\Lambda}$, and η are all reconstructed. The threshold enhancement can also be observed but it is not as significant as that observed with the partial reconstruction technique. In addition, a small peak from the process $e^+e^- \to J/\psi\eta \to \Lambda\bar{\Lambda}\eta$ at 3.1 GeV/c^2 can be seen in Fig. 6. Currently, the peak around 2.8 GeV/c^2 cannot be taken into account because the significance for the structure is low and there is no well-established resonance decaying into $\Lambda\bar{\Lambda}$ with mass around 2.8 GeV/c^2 in the PDG [6].

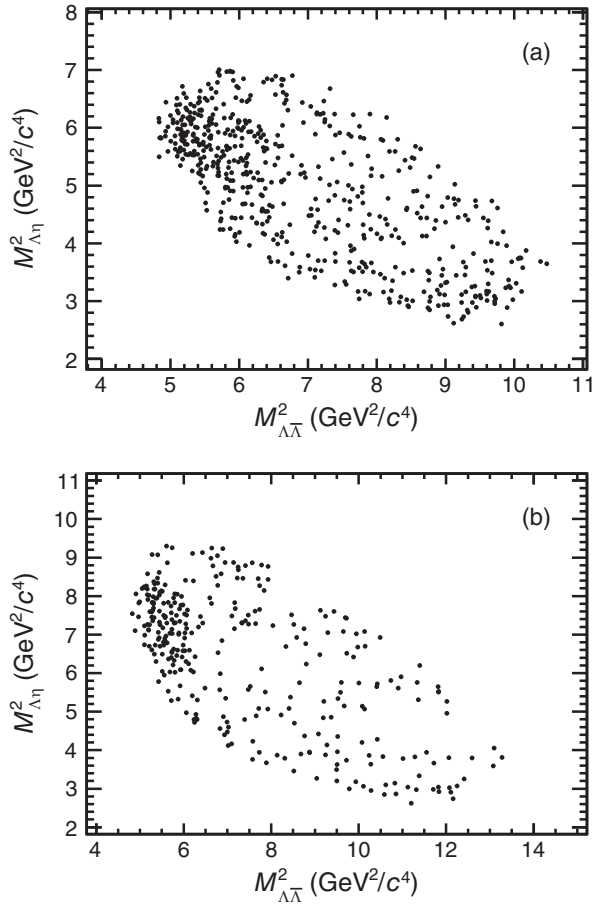

FIG. 5. Dalitz plots of $M^2_{\Lambda\eta}$ versus $M^2_{\Lambda\bar{\Lambda}}$ in data taken at (a) $\sqrt{s} = 3.7730$ GeV and (b) $\sqrt{s} = 4.1784$ GeV.

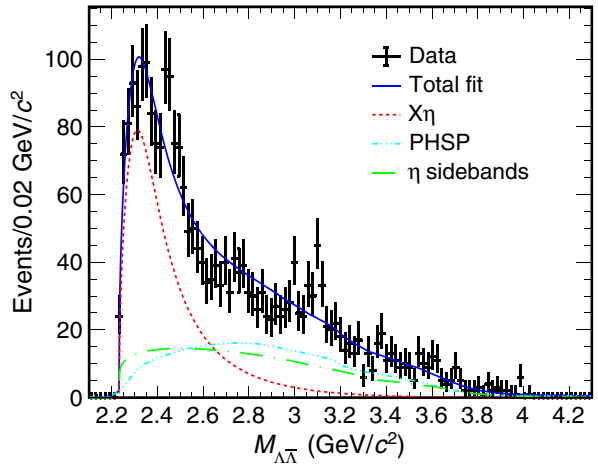

FIG. 6. Sum of the simultaneous fits to the $M_{\Lambda\bar{\Lambda}}$ distributions at the 31 energy points. The black points with error bars are data. The solid blue curve shows the total fit. The dashed red line is the enhancement. The dash-dotted cyan line shows PHSP component. The long dashed-dotted green line denotes the background component.

To determine the mass and width of the enhancement, a simultaneous unbinned maximum-likelihood fit is performed to the $\Lambda\bar{\Lambda}$ invariant mass spectra of the data samples at the 31 energy points. The enhancement is modeled by a Breit-Wigner function with mass-dependent width of the following form [72]:

$$\mathrm{d}N/\mathrm{d}M_{\Lambda\bar{\Lambda}} \propto \varepsilon(M_{\Lambda\bar{\Lambda}})(p_X)^{2l_{X\eta}+1} f^2_{l_{X\eta}}((Rp_X)^2)|\mathrm{BW}(M_{\Lambda\bar{\Lambda}})|^2 \times (p_\Lambda)^{2l_{\Lambda\bar{\Lambda}}+1} f^2_{l_{\Lambda\bar{\Lambda}}}((Rp_\Lambda)^2), \quad (4)$$

where X denotes the threshold enhancement, the mass-dependent reconstruction efficiency $\varepsilon(M_{\Lambda\bar{\Lambda}})$ is determined by the MC simulation, p_X is the momentum of X in the e^+e^- center-of-mass system, $l_{X\eta}$ is the orbital angular momentum between X and η, and $f_l(z)$ is the Blatt-Weisskopf barrier factor [73] with $f_0(z) = 1$ and $f_1(z) = \frac{1}{\sqrt{1+z}}$, where l is the orbital angular momentum. The barrier radius factor R is assumed to be 1.0 $(\mathrm{GeV}/c)^{-1}$ since it is poorly known for baryons. The Breit-Wigner amplitude is defined as

$$\mathrm{BW} \propto \frac{1}{M_X^2 - M^2_{\Lambda\bar{\Lambda}} - iM_X\Gamma}, \quad (5)$$

where M_X is the mass of X. The mass-dependent width Γ is written as

$$\Gamma = \Gamma_X \left(\frac{p_\Lambda}{p^X_\Lambda}\right)^{2l_{\Lambda\bar{\Lambda}}+1} \frac{M_X}{M_{\Lambda\bar{\Lambda}}} \frac{f^2_{l_{\Lambda\bar{\Lambda}}}((Rp_\Lambda)^2)}{f^2_{l_{\Lambda\bar{\Lambda}}}((Rp^X_\Lambda)^2)}, \quad (6)$$

where Γ_X is the width of X, p_Λ is the momentum of Λ in the rest frame of X, p^X_Λ is the momentum when $M_{\Lambda\bar{\Lambda}} = M_X$, and $l_{\Lambda\bar{\Lambda}}$ is the orbital angular momentum between Λ and $\bar{\Lambda}$. In the simultaneous fit, M_X and Γ_X are the common parameters. Based on the conservation of angular momentum, parity, and charge conjugation, the possible quantum numbers of the enhancement are listed in Table II, which summarizes the possible combinations of $l_{\Lambda\bar{\Lambda}}$ and $l_{X\eta}$. We assume the structure has J^{PC} equal to 1^{--} and $l_{\Lambda\bar{\Lambda}}$ equal to 0 since the enhancement is near the $\Lambda\bar{\Lambda}$ mass threshold.

We use MC simulations of the process $e^+e^- \to \Lambda\bar{\Lambda}\eta$ to determine $\varepsilon(M_{\Lambda\bar{\Lambda}})$, where the mass distribution of the $\Lambda\bar{\Lambda}$ system follows a Breit-Wigner function with a relatively

TABLE II. Possible quantum numbers of X considering conservation of angular momenta, parity, and charge conjugation, where $S_{\Lambda\bar{\Lambda}}$ is the total spin of $\Lambda\bar{\Lambda}$ system.

$S_{\Lambda\bar{\Lambda}}/l_{\Lambda\bar{\Lambda}}$ of $\Lambda\bar{\Lambda}$	J^{PC} of X	$l_{X\eta}$
0/1	1^{+-}	0
0/1	1^{+-}	2
1/0	1^{--}	1
1/2	1^{--}	1
1/2	2^{--}	1

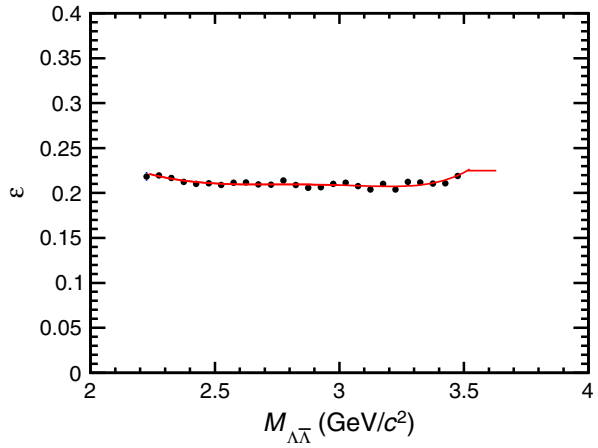

FIG. 7. Fit to the mass-dependent efficiency $\varepsilon(M_{\Lambda\bar{\Lambda}})$ (the black points) at $\sqrt{s} = 4.1784$ GeV. The red line in the region $M_{\Lambda\bar{\Lambda}} < 3.5$ GeV/c^2 represents the fit result which is a sixth-order polynomial function. The red line in the region $M_{\Lambda\bar{\Lambda}} > 3.5$ GeV/c^2 is the extrapolation. The efficiency is obtained from the distribution of the reconstructed value of $M_{\Lambda\bar{\Lambda}}$ divided by the distribution of the generated value of $M_{\Lambda\bar{\Lambda}}$.

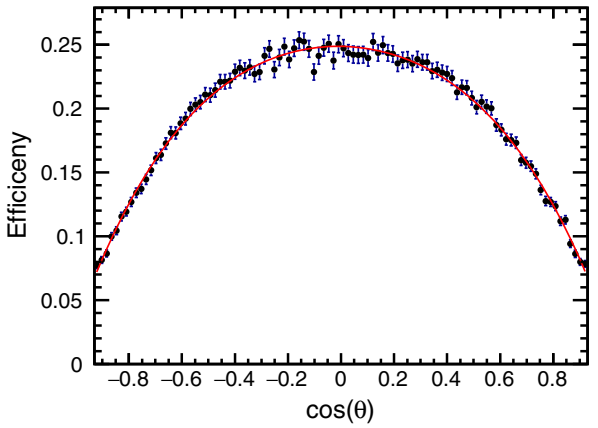

FIG. 8. Fit to the $\varepsilon(\cos\theta)$ (the black points) at $\sqrt{s} = 4.1784$ GeV. The red line represents the fit result which is a fourth-order polynomial function. The efficiency is obtained from the MC simulation.

large width so that the $M_{\Lambda\bar{\Lambda}}$ distribution is uniform within the allowed region. The quantum numbers are configured according to the assumption in the previous paragraph. Figure 7 shows $\varepsilon(M_{\Lambda\bar{\Lambda}})$ as a function of $M_{\Lambda\bar{\Lambda}}$ at $\sqrt{s} = 4.1784$ GeV with $M_{\Lambda\bar{\Lambda}} < 3.5$ GeV/c^2. We parametrize $\varepsilon(M_{\Lambda\bar{\Lambda}})$ by a sixth-order polynomial function. Because of the detector resolution, the reconstructed distributions exceed the allowed region. As a result, the efficiency cannot be determined correctly in the range of $M_{\Lambda\bar{\Lambda}} > 3.5$ GeV/c^2, which is not included in the parametrization. Instead, the efficiency in this region, which is far away from the threshold enhancement, is estimated by a flat extrapolation assuming the efficiency is constant in the region.

The events from the nonresonant process $e^+e^- \to \Lambda\bar{\Lambda}\eta$ are described by shapes derived from the PHSP MC samples. The background events are modeled by the formula [74]

$$f(M_{\Lambda\bar{\Lambda}}) \propto (M_{\Lambda\bar{\Lambda}} - M_{\rm min})^l (M_{\rm max} - M_{\Lambda\bar{\Lambda}})^h, \qquad (7)$$

where $M_{\rm min} = 2M_\Lambda$ is the minimum allowed $M_{\Lambda\bar{\Lambda}}$, $M_{\rm max} = \sqrt{s} - M_\eta$ is the maximum allowed $M_{\Lambda\bar{\Lambda}}$ calculated with center-of-mass energy $\sqrt{s}$ and known mass of η, M_η [6], and l and h are determined by fitting the $M_{\Lambda\bar{\Lambda}}$ spectra of events from the η sidebands. The magnitudes of the background shapes are fixed to the number of the fitted background events within the η signal region.

Figure 6 shows the sum of the simultaneous fit to the $M_{\Lambda\bar{\Lambda}}$ spectra at the 31 energy points. The mass and width of X obtained from the fit are (2356 ± 7) MeV/c^2 and (304 ± 28) MeV, respectively, where the uncertainties are statistical only. In the fit, the excited Λ states are not included because they are not significant in the data (Fig. 5) and are not well established [6]. Recently, an improved measurement of $\Lambda(1670)$ via the $\psi(2S) \to \Lambda\bar{\Lambda}\eta$ decay has been reported by the BESIII Collaboration [40]. The effect of the $\Lambda(1670)$ on the determination of mass and width will be discussed in Sec. VI B for the estimation of systematic uncertainties. Because of the limited sample sizes, the potential interferences among the threshold enhancement, excited Λ states, and three-body PHSP component are neglected. The combined statistical signal significance is greater than 10σ, which is determined by the difference of likelihood values between the fit with and without the model for the enhancement [75].

In the determination of mass and width of X, $l_{X\eta}$ is assumed to be one. The $\cos\theta$ distributions of η candidates should follow the distribution of $(1 + \cos^2\theta)$ when $l_{X\eta} = 1$. Therefore, the angular distributions of X decays are studied to verify this assumption. We perform a simultaneous unbinned maximum-likelihood fit to the $\cos\theta$ distributions at the 31 center-of-mass energies. The $\cos\theta$ distributions of X decays are modeled by the function $\varepsilon(\cos\theta)(1 + \alpha\cos^2\theta)$, where the parameter α is free and taken as a common parameter. The reconstruction efficiency $\varepsilon(\cos\theta)$ is parametrized by a fourth-order polynomial function. The fourth-order polynomial function for the data taken at 4.1784 GeV is shown in Fig. 8. The shape of the PHSP process is modeled by the MC simulations. The background contributions are described by the shapes derived from the η sidebands. In the fit, the numbers of events for the three components are fixed to the values obtained from the simultaneous fit to the $M_{\Lambda\bar{\Lambda}}$ distributions. Figure 9 shows the sum of the simultaneous fit to the distributions of $\cos\theta$. The parameter α is determined to be 0.8 ± 0.3, which is consistent with our assumption of $\alpha = 1$ considering the statistical uncertainty.

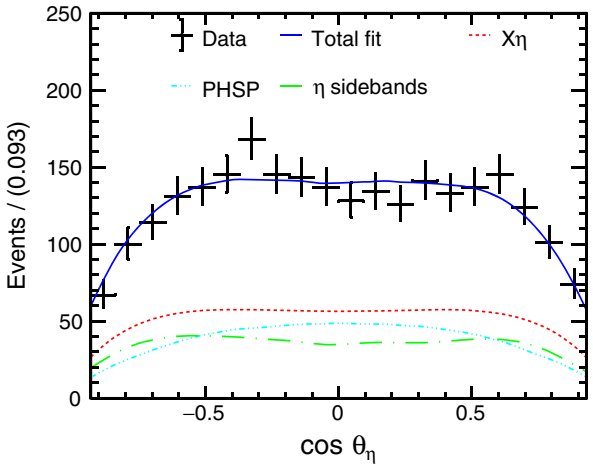

FIG. 9. Sum of the simultaneous fits to the $\cos\theta$ distributions of η candidates at the 31 energy points. The black points with error bars are the data. The solid blue line shows the total fit. The dashed red line shows the X component, and the dashed cyan line denotes the PHSP component. The dashed green line is the background.

VI. SYSTEMATIC UNCERTAINTIES

A. Born cross section measurement

According to Eq. (1), the uncertainties on the cross section measurement are associated with the luminosity, branching fractions, reconstruction efficiency, fit procedure, ISR correction, and vacuum polarization factor. The uncertainty of the reconstruction efficiency includes contributions from the Λ reconstruction, PID of the pion, photon reconstruction, shower requirements, Σ^0 mass window, and weighting procedure (limited data sample sizes, binning of data distributions, η mass window, and η sidebands). The uncertainty of the fit procedure incorporates the fit range, background shape, peaking background, and signal shape. To reduce the effect of statistical uncertainty due to limited sample sizes, we take the samples at 3.7730 and 4.1784 GeV (the two samples with the highest luminosities) to estimate the uncertainties from the Λ reconstruction, Σ^0 mass window, weighting of PHSP MC samples (except for the limited data sample size), and fit procedure.

(1) *Luminosity.*—The uncertainties from the integrated luminosities measured using the large-angle Bhabha events are assigned to be 1.0% [64–66].

(2) *Branching fractions.*—The systematic uncertainty due to the branching fractions $\mathcal{B}(\eta \to \gamma\gamma)$ and $\mathcal{B}(\Lambda \to p\pi^-)$ are 0.5% and 0.8%, respectively, taken from the PDG [6].

(3) Λ *reconstruction.*—The systematic uncertainty from the Λ ($\bar{\Lambda}$) reconstruction efficiency is estimated with the equation [76]

$$\left|\frac{\Sigma_i \frac{N_i}{\varepsilon_i^{\rm Data}} - \Sigma_i \frac{N_i}{\varepsilon_i^{\rm MC}}}{\Sigma_i \frac{N_i}{\varepsilon_i^{\rm MC}}}\right|, \tag{8}$$

where N_i is the number of data events in the interval i with background subtracted using the η sidebands and $\varepsilon_i^{\rm Data}$ and $\varepsilon_i^{\rm MC}$ are the efficiencies of Λ ($\bar{\Lambda}$) reconstruction for the data and MC simulations, respectively, in interval i of the two-dimensional (momentum and $\cos\theta$) distributions. The efficiencies are determined by a control sample of $J/\psi \to \bar{p}K^+\Lambda + \text{c.c.}$ [77]. It takes the tracking of proton and pion, PID of proton, mass window for Λ ($\bar{\Lambda}$) candidates, and the requirement on the decay length into account. The uncertainty is estimated to be 2.8%.

(4) *PID of pion.*—The uncertainty introduced by the PID of the pion is estimated to be 1.0% by a control sample of $e^+e^- \to K^+K^-\pi^+\pi^-$ [78].

(5) *Photon reconstruction.*—A systematic uncertainty of 1.0% [79] is assigned to the photon reconstruction efficiency. Hence, 2.0% is taken as the systematic uncertainty for two photons.

(6) *Shower requirements.*—The uncertainty associated with the requirements on the lateral moment and $E_{3\times3}/E_{5\times5}$ is 0.8% [80].

(7) Σ^0 *mass window.*—The requirement $M_{\Lambda\gamma_L(\bar{\Lambda}\gamma_L)} \notin [1.113, 1.273]\ \text{GeV}/c^2$ is applied to suppress the background processes with Σ^0 ($\bar{\Sigma}^0$) in the final state. By changing the width of the nominal mass window by $\pm 25\ \text{MeV}/c^2$, the corresponding uncertainty is estimated to be 1.2%.

(8) *Weighting procedure.*—Using the $M_{\Lambda\bar{\Lambda}}$, $M_{\Lambda\eta}$, and $M_{\bar{\Lambda}\eta}$ distributions from the data events, the PHSP MC is weighted to determine the reconstruction efficiency.

(a) *Limited data sample size.*—To estimate the uncertainties caused by the statistical fluctuation of the background-subtracted data distributions, we first produce a series of $M_{\Lambda\bar{\Lambda}}$, $M_{\Lambda\eta}$, and $M_{\bar{\Lambda}\eta}$ distributions for each energy point by sampling over the three background-subtracted data distributions with Poisson functions. The means of the Poisson functions are the number of events in the intervals of the three background-subtracted data distributions. The PHSP MC samples are then weighted by the generated $M_{\Lambda\bar{\Lambda}}$, $M_{\Lambda\eta}$, and $M_{\bar{\Lambda}\eta}$ distributions. The means and standard deviations of the resulting efficiency distributions are taken as efficiencies and corresponding uncertainties from limited data sample sizes, respectively.

(b) *Binning of data distributions.*—The widths of intervals in the $M_{\Lambda\bar{\Lambda}}$, $M_{\Lambda\eta}$, and $M_{\bar{\Lambda}\eta}$ distributions are changed by a factor of 2 of nominal width to estimated corresponding uncertainties. The resulting relative difference in the efficiency is assigned as corresponding uncertainty, which is 0.6%.

(c) *η mass window.*—The width of the η mass window is varied by $\pm 16\ \mathrm{MeV}/c^2$ (twice the resolution of the invariant mass of the η candidates) to estimate the corresponding uncertainty, which is 1.0%.

(d) *η sidebands.*—To estimate the uncertainty due to the sidebands, their distances to the signal region are varied by $\pm 8\ \mathrm{MeV}/c^2$. The corresponding uncertainty is found to be negligible.

(9) *Fit procedure.*—The signal yield is determined by an unbinned maximum-likelihood fit to the $M_{\gamma\gamma}$ spectrum. The following aspects are considered when evaluating the systematic uncertainties associated with the fit procedure.

(a) *Fit range.*—The ranges of fits to the $M_{\gamma\gamma}$ distributions are varied by $\pm 100\ \mathrm{MeV}/c^2$. The resulting relative difference in the signal yield is taken as the corresponding uncertainty. The uncertainty is taken as 0.9%.

(b) *Background shape.*—The nominal background shape, a linear function, is replaced by a second-order Chebychev polynomial. The estimated uncertainty is 1.6%.

(c) *Peak background.*—For the peaking background from the processes $e^+e^- \to \eta\Sigma^0\bar{\Lambda}$ + c.c. and $e^+e^- \to \eta\Sigma^0\bar{\Sigma}^0$, we add the shapes of the two processes obtained from the MC simulations to the nominal model. The corresponding uncertainty is estimated to be 2.9%.

(d) *Signal shape.*—For the signal shape, we set the fixed width of the Gaussian function to be free in the nominal fit. The corresponding uncertainty is estimated to be 0.5%.

(10) *ISR correction.*—For uncertainties from ISR correction factors, we replace the smoothing method LOWESS [70] by the power-law function C/s^{λ}, where the parameters C and λ are determined by fitting the measured Born cross section. The relative changes with respect to the nominal cross sections are assigned as the systematic uncertainties summarized in Table III.

(11) *Vacuum polarization factor.*—The uncertainty introduced by the vacuum polarization factor is less than 0.1% [67], which is negligible compared to other sources of uncertainties.

Table IV summarizes the uncertainties for all the samples.

TABLE III. Relative uncertainties (%) from ISR correction in the measurement of the Born cross section.

$\sqrt{s}$ (GeV)	Uncertainty	$\sqrt{s}$ (GeV)	Uncertainty
3.5106	0.1	4.2879	1.4
3.7730	0.3	4.3121	1.7
3.8720	1.4	4.3374	0.9
4.0076	0.5	4.3583	1.7
4.1285	2.1	4.3774	3.4
4.1574	2.3	4.3964	4.5
4.1784	3.0	4.4156	2.4
4.1888	2.4	4.4400	8.2
4.1989	1.4	4.4671	6.2
4.2092	0.8	4.5995	5.6
4.2187	0.7	4.6280	2.6
4.2263	1.2	4.6612	2.0
4.2357	1.0	4.6409	2.8
4.2438	1.2	4.6819	3.4
4.2580	1.2	4.6988	3.9
4.2668	3.8		

TABLE IV. Systematic uncertainties in the measurement of the Born cross section.

Source	Uncertainty
Luminosity	1.0%
$\mathcal{B}(\eta \to \gamma\gamma)$ and $\mathcal{B}(\Lambda \to p\pi^-)$	0.9%
Λ reconstruction	2.8%
PID of pion	1.0%
Photon reconstruction	2.0%
Shower requirements	0.8%
Σ^0 mass window	1.2%
Limited data sample size	See Table I
Binning of data distributions	0.6%
η mass window	1.0%
η sidebands	Negligible
Fit range	0.9%
Background shape	1.6%
Peaking background	2.9%
Signal shape	0.5%
ISR correction	See Table III

B. Mass and width of the threshold enhancement

The mass and width of the threshold enhancement in the $\Lambda\bar{\Lambda}$ mass spectra are determined by the simultaneous unbinned maximum-likelihood fit. The uncertainties associated with the mass and width are assigned as follows.

(1) *Description of the threshold enhancement.*—In the simultaneous fit to the $M_{\Lambda\bar{\Lambda}}$ distributions, the barrier radius is assumed to be 1.0. To determine the uncertainties from the assumption, the simultaneous fit is repeated with the barrier radius being free, which results in a mass difference of 1 MeV/c^2 and a width difference of 4 MeV. The uncertainties due to the parametrization of efficiency curves $\varepsilon(m_{\Lambda\bar{\Lambda}})$ are estimated by replacing the sixth-order polynomial function with a seventh-order polynomial function. The resulting differences in the mass and width are negligible.

(2) *Background shape.*—The uncertainties related to the background description are estimated by changing Eq. (7) to the shapes of histograms obtained from events in η sidebands of the data. A fit under the

scenario yields a mass difference of 5 MeV/c^2 and a width difference of 11 MeV.

(3) $e^+e^- \to J/\psi\eta \to \Lambda\bar{\Lambda}\eta$.—In the $\Lambda\bar{\Lambda}$ mass spectrum shown in Fig. 3, there is a small peak at the J/ψ mass from the process $e^+e^- \to J/\psi\eta \to \Lambda\bar{\Lambda}\eta$. To estimate the effect of this process on the determination of mass and width of the threshold enhancement, we add the shape obtained from the MC simulation of $e^+e^- \to J/\psi\eta \to \Lambda\bar{\Lambda}\eta$ to the nominal fit model. The differences in the mass and width are 1 MeV/c^2 and 1 MeV, respectively.

(4) $e^+e^- \to \Lambda(1670)\bar{\Lambda} + \text{c.c.} \to \Lambda\bar{\Lambda}\eta$.—To consider the effect of the excited Λ state $\Lambda(1670)$ on the measurement of mass and width, we add the shape of the process obtained from the MC simulation to the nominal model. The resulting differences in mass and width, which are 11 MeV/c^2 and 48 MeV, respectively, to the nominal results are assigned as corresponding uncertainties.

(5) Σ^0 *mass window,* η *mass window, and* η *sidebands.*—The Σ^0 mass window, η mass window, and η sidebands are altered as mentioned in Sec. VI A, to estimate corresponding uncertainties. The maximum differences in mass are 3, 9, and 0.1 MeV/c^2, and the maximum differences in width are 10, 20, and 1 MeV, which are assigned as corresponding systematic uncertainties.

After adding these uncertainties in quadrature, the total systematic uncertainties on the mass and width of the enhancement are determined to be 15 MeV/c^2 and 54 MeV, respectively.

VII. SUMMARY

Based on the 31 data samples taken at the center-of-mass energies from 3.51 to 4.70 GeV, we measure the Born cross section of the process $e^+e^- \to \Lambda\bar{\Lambda}\eta$, as shown in Table I. No significant structure is observed in the line shape of the Born cross section, which can be described by a power-law function C/s^{λ} with $C = (4.0 \pm 2.5) \times 10^3$ GeV$^{2\lambda}$ pb and $\lambda = 2.9 \pm 0.2$.

Further, a clear enhancement above pure phase space is observed near the $\Lambda\bar{\Lambda}$ mass threshold. The contributions of the excited Λ are neglected in the study of $M_{\Lambda\bar{\Lambda}}$ distribution since they are not significant in the data and are not well established [6]. Because of the limited data sample sizes, the potential interferences among the structure, excited Λ states, and phase space process are also not considered. A simultaneous fit to the $\Lambda\bar{\Lambda}$ mass spectra, assuming $J^{PC} = 1^{--}$, yields a mass of $(2356 \pm 7 \pm 15)$ MeV/c^2 and width of $(304 \pm 28 \pm 54)$ MeV for the structure. The first uncertainties are statistical and the second are systematic. The statistical signal significance of the structure is larger than 10σ over the hypothesis of the pure contribution from the PHSP process of $e^+e^- \to \Lambda\bar{\Lambda}\eta$. The $\cos\theta$ distributions of the structure can be described by a function of $(1 + \alpha\cos^2\theta)$. A simultaneous fit to the $\cos\theta$ distributions gives $\alpha = 0.8 \pm 0.3$ which is consistent with our assumption of $\alpha = 1$, where the uncertainty is statistical only. In the PDG, there is no well-established resonance matching the structure in terms of the resonance parameters. A vector hexaquark state decaying into $\Lambda\bar{\Lambda}$ is proposed with a mass of 2200 MeV/c^2 and a width of 32 MeV [81]. The mass is close to our measurement but the width of the hexaquark state is much narrower than the width of the observed structure. In the framework of QCD sum rules, an investigation of light baryonium states indicates that there exist possible light baryonium states, including the $\Lambda\bar{\Lambda}$ state with J^{PC} of 1^{--} [82]. The mass for the $\Lambda\bar{\Lambda}$ state is evaluated to be 2.34 ± 0.12 GeV/c^2, which is consistent with our measurement. For the structure with $M = 2290 \pm 20$ MeV/c^2 and $\Gamma = 275 \pm 35$ MeV observed with a partial wave analysis of PS185 data [19], the width is consistent with our result within the uncertainties, while the mass difference is greater than 2σ. For the recently observed near-threshold enhancement in the process $e^+e^- \to \phi\Lambda\bar{\Lambda}$ [72], its C parity is opposite to the enhancement in our analysis. The measured values of mass and width are $(2262 \pm 4 \pm 28)$ MeV/c^2 and $(72 \pm 5 \pm 43)$ MeV, respectively, which are smaller than the mass and width of our measurements. A future larger data sample [83] and theories incorporating a partial wave analysis could lead to a better understanding of the observed structure.

ACKNOWLEDGMENTS

The BESIII Collaboration thanks the staff of BEPCII and the IHEP computing center for their strong support. This work is supported in part by National Key R&D Program of China under Contracts No. 2020YFA0406300 and No. 2020YFA0406400; National Natural Science Foundation of China (NSFC) under Contracts No. 11635010, No. 11735014, No. 11835012, No. 11935015, No. 11935016, No. 11935018, No. 11961141012, No. 12022510, No. 12025502, No. 12035009, No. 12035013, No. 12192260, No. 12192261, No. 12192262, No. 12192263, No. 12192264, and No. 12192265; the Chinese Academy of Sciences (CAS) Large-Scale Scientific Facility Program; the CAS Center for Excellence in Particle Physics (CCEPP); Joint Large-Scale Scientific Facility Funds of the NSFC and CAS under Contract No. U1832207; CAS Key Research Program of Frontier Sciences under Contracts No. QYZDJ-SSW-SLH003 and No. QYZDJ-SSW-SLH040; 100 Talents Program of CAS; The Institute of Nuclear and Particle Physics (INPAC) and Shanghai Key Laboratory for Particle Physics and Cosmology; ERC under Contract No. 758462; European Union's Horizon 2020 research and innovation program under Marie Sklodowska-Curie grant agreement under Contract No. 894790; German Research Foundation

DFG under Contracts No. 443159800 and No. 455635585, Collaborative Research Center CRC 1044, FOR5327, and GRK 2149; Istituto Nazionale di Fisica Nucleare, Italy; Ministry of Development of Turkey under Contract No. DPT2006K-120470; National Science and Technology fund; National Science Research and Innovation Fund (NSRF) via the Program Management Unit for Human Resources & Institutional Development, Research and Innovation under Contract No. B16F640076; Olle Engkvist Foundation under Contract No. 200-0605; STFC (United Kingdom); Suranaree University of Technology (SUT), Thailand Science Research and Innovation (TSRI), and National Science Research and Innovation Fund (NSRF) under Contract No. 160355; The Royal Society, United Kingdom under Contracts No. DH140054 and No. DH160214; The Swedish Research Council; and U.S. Department of Energy under Contract No. DE-FG02-05ER41374.

[1] B. Aubert *et al.* (*BABAR* Collaboration), Phys. Rev. Lett. **95**, 142001 (2005).
[2] Q. He *et al.* (CLEO Collaboration), Phys. Rev. D **74**, 091104 (2006).
[3] C. Z. Yuan *et al.* (Belle Collaboration), Phys. Rev. Lett. **99**, 182004 (2007).
[4] N. Brambilla, S. Eidelman, C. Hanhart, A. Nefediev, C.-P. Shen, C. E. Thomas, A. Vairo, and C.-Z. Yuan, Phys. Rep. **873**, 1 (2020).
[5] M. B. Voloshin, Prog. Part. Nucl. Phys. **61**, 455 (2008).
[6] R. L. Workman *et al.* (Particle Data Group), Prog. Theor. Exp. Phys. **2022**, 083C01 (2022).
[7] M. Ablikim *et al.* (BESIII Collaboration), Phys. Rev. Lett. **118**, 092001 (2017).
[8] B. Aubert *et al.* (*BABAR* Collaboration), Phys. Rev. Lett. **98**, 212001 (2007).
[9] X. L. Wang *et al.* (Belle Collaboration), Phys. Rev. Lett. **99**, 142002 (2007).
[10] S. L. Zhu, Phys. Lett. B **625**, 212 (2005).
[11] M. Ablikim *et al.* (BESIII Collaboration), Phys. Lett. B **771**, 45 (2017).
[12] M. Ablikim *et al.* (BESIII Collaboration), Phys. Rev. D **99**, 072005 (2019).
[13] M. Ablikim *et al.* (BESIII Collaboration), Phys. Rev. D **99**, 012003 (2019).
[14] M. Ablikim *et al.* (BESIII Collaboration), Phys. Rev. D **99**, 012014 (2019).
[15] M. Ablikim *et al.* (BESIII Collaboration), Phys. Rev. Lett. **124**, 032002 (2020).
[16] M. Ablikim *et al.* (BESIII Collaboration), Phys. Rev. D **103**, 052003 (2021).
[17] M. Ablikim *et al.* (BESIII Collaboration), Phys. Rev. D **104**, L091104 (2021).
[18] M. Ablikim *et al.* (BESIII Collaboration), J. High Energy Phys. 07 (2022) 064.
[19] D. V. Bugg, Eur. Phys. J. C **36**, 161 (2004).
[20] J. Bai *et al.* (BES Collaboration), Phys. Rev. Lett. **91**, 022001 (2003).
[21] Y. W. Chang *et al.* (Belle Collaboration), Phys. Rev. D **79**, 052006 (2009).
[22] B. Aubert *et al.* (*BABAR* Collaboration), Phys. Rev. D **79**, 112009 (2009).
[23] J. T. Wei *et al.* (Belle Collaboration), Phys. Lett. B **659**, 80 (2008).
[24] Y. W. Chang *et al.* (Belle Collaboration), Phys. Rev. D **79**, 052006 (2009).
[25] J. H. Chen *et al.* (Belle Collaboration), Phys. Rev. Lett. **100**, 251801 (2008).
[26] P. del Amo Sanchez *et al.* (*BABAR* Collaboration), Phys. Rev. D **85**, 092017 (2012).
[27] Y. Y. Chang *et al.* (Belle Collaboration), Phys. Rev. Lett. **115**, 221803 (2015).
[28] R. Aaij *et al.* (LHCb Collaboration), Phys. Rev. D **96**, 051103 (2017).
[29] P. C. Lu *et al.* (Belle Collaboration), Phys. Rev. D **99**, 032003 (2019).
[30] B. Pal *et al.* (Belle Collaboration), Phys. Rev. D **99**, 091104 (2019).
[31] R. Aaij *et al.* (LHCb Collaboration), J. High Energy Phys. 03 (2020) 146.
[32] J. P. Alexander *et al.* (CLEO Collaboration), Phys. Rev. D **82**, 092002 (2010).
[33] M. Ablikim *et al.* (BESIII Collaboration), Phys. Rev. Lett. **110**, 022001 (2013).
[34] S. B. Athar *et al.* (CLEO Collaboration), Phys. Rev. D **73**, 032001 (2006).
[35] M. Ablikim *et al.* (BESIII Collaboration), Phys. Rev. D **87**, 112004 (2013).
[36] M. Ablikim *et al.* (BESIII Collaboration), Phys. Rev. D **88**, 032010 (2013).
[37] M. Ablikim *et al.* (BESIII Collaboration), Phys. Rev. D **93**, 052010 (2016).
[38] M. Ablikim *et al.* (BESIII Collaboration), Phys. Rev. D **99**, 112010 (2019).
[39] M. Ablikim *et al.* (BESIII Collaboration), Phys. Rev. D **106**, 112007 (2022).
[40] M. Ablikim *et al.* (BESIII Collaboration), Phys. Rev. D **106**, 072006 (2022).
[41] M. Ablikim *et al.* (BESIII Collaboration), Phys. Rev. D **106**, 112011 (2022).
[42] R. Aaij *et al.* (LHCb Collaboration), Eur. Phys. J. C **73**, 2462 (2013).
[43] J. P. Lees *et al.* (*BABAR* Collaboration), Phys. Rev. D **89**, 112002 (2014).
[44] K. Chu *et al.* (Belle Collaboration), Phys. Rev. D **101**, 052012 (2020).
[45] R. Aaij *et al.* (LHCb Collaboration), Phys. Rev. Lett. **128**, 062001 (2022).

[46] R. Aaij *et al.* (LHCb Collaboration), arXiv:2210.10346.
[47] J. L. Rosner, Phys. Rev. D **68**, 014004 (2003).
[48] C. R. Deng, J. L. Ping, Y. C. Yang, and F. Wang, Phys. Rev. D **88**, 074007 (2013).
[49] G. J. Ding, J. L. Ping, and M. L. Yan, Phys. Rev. D **74**, 014029 (2006).
[50] O. D. Dalkarov, P. A. Khakhulin, and A. Y. Voronin, Nucl. Phys. **A833**, 104 (2010).
[51] M. Ablikim *et al.* (BESIII Collaboration), Nucl. Instrum. Methods Phys. Res., Sect. A **614**, 345 (2010).
[52] C. H. Yu *et al.*, *Proceedings of the IPAC2016, Busan, Korea, 2016* (JACoW, Geneva, Switzerland, 2016).
[53] P. Cao *et al.*, Nucl. Instrum. Methods Phys. Res., Sect. A **953**, 163053 (2020).
[54] S. Agostinelli *et al.* (GEANT4 Collaboration), Nucl. Instrum. Methods Phys. Res., Sect. A **506**, 250 (2003).
[55] S. Jadach, B. F. L. Ward, and Z. Was, Phys. Rev. D **63**, 113009 (2001); Comput. Phys. Commun. **130**, 260 (2000).
[56] D. J. Lange, Nucl. Instrum. Methods Phys. Res., Sect. A **462**, 152 (2001); R. G. Ping, Chin. Phys. C **32**, 599 (2008).
[57] J. C. Chen, G. S. Huang, X. R. Qi, D. H. Zhang, and Y. S. Zhu, Phys. Rev. D **62**, 034003 (2000); R. L. Yang, R. G. Ping, and H. Chen, Chin. Phys. Lett. **31**, 061301 (2014).
[58] E. Richter-Was, Phys. Lett. B **303**, 163 (1993).
[59] M. Xu *et al.*, Chin. Phys. C **33**, 428 (2009).
[60] A. Drescher, B. Grawe, B. Hahn, B. Ingelbach, U. Matthiesen, H. Scheck, J. Spengler, and D. Wegener, Nucl. Instrum. Methods Phys. Res., Sect. A **237**, 464 (1985).
[61] M. He, J. Phys. Conf. Ser. **293**, 012025 (2011).
[62] D. Asner *et al.*, Int. J. Mod. Phys. A **24**, S1 (2009), https://www.worldscientific.com/toc/ijmpa/24/supp01.
[63] X. Zhou, S. Du, G. Li, and C. Shen, Comput. Phys. Commun. **258**, 107540 (2021).
[64] M. Ablikim *et al.* (BESIII Collaboration), Chin. Phys. C **39**, 093001 (2015).
[65] M. Ablikim *et al.* (BESIII Collaboration), Chin. Phys. C **46**, 113002 (2022).
[66] M. Ablikim *et al.* (BESIII Collaboration), Chin. Phys. C **46**, 113003 (2022).
[67] F. Jegerlehner, Nuovo Cimento C **034S1**, 31 (2011).
[68] M. Ablikim *et al.* (BESIII Collaboration), Chin. Phys. C **45**, 103001 (2021).
[69] W. Y. Sun, T. Liu, M. Q. Jing, L. L. Wang, B. Zhong, and W. M. Song, Front. Phys. **16**, 64501 (2021).
[70] W. Cleveland, Am. Stat. **35**, 54 (1981), https://www.bibsonomy.org/bibtex/2843ccdc7ff9d98be1400e2ec3340fbad/ar0berts.
[71] M. Ablikim *et al.* (BESIII Collaboration), Phys. Lett. B **771**, 45 (2017).
[72] M. Ablikim *et al.* (BESIII Collaboration), Phys. Rev. D **104**, 052006 (2021).
[73] A. Abulencia *et al.* (CDF Collaboration), Phys. Rev. Lett. **96**, 102002 (2006).
[74] M. Ablikim *et al.* (BESIII Collaboration), Phys. Rev. D **92**, 092006 (2015).
[75] Y. S. Zhu, High Energy Phys. Nucl. Phys.**30**, 331 (2006), arXiv:0812.2708.
[76] M. Ablikim *et al.* (BESIII Collaboration), Phys. Rev. D **99**, 032010 (2019).
[77] M. Ablikim *et al.* (BESIII Collaboration), Phys. Rev. Lett. **121**, 062003 (2018).
[78] M. Ablikim *et al.* (BESIII Collaboration), Phys. Rev. D **104**, 052006 (2021).
[79] M. Ablikim *et al.* (BESIII Collaboration), Phys. Rev. D **81**, 052005 (2010).
[80] M. Ablikim *et al.* (BESIII Collaboration), Phys. Rev. D **95**, 111102 (2017).
[81] S. M. Gerasyuta and E. E. Matskevich, Int. J. Mod. Phys. E **29**, 2050035 (2020).
[82] B.-D. Wan, S.-Q. Zhang, and C.-F. Qiao, Phys. Rev. D **105**, 014016 (2022).
[83] M. Ablikim *et al.* (BESIII Collaboration), Chin. Phys. C **44**, 040001 (2020).